Electronic Supplementary Material (ESI) for Materials Horizons.
This journal is © The Royal Society of Chemistry 2023

**Electronic Supplementary Information**

# Nanocomposite Conductive Hydrogels with Robust Elasticity and Multifunctional Responsiveness for Flexible Sensing and Wound Monitoring

*Kaixiang Shen,[a] Zheng Liu,[a] Ruilin Xie,[a] Yuchen Zhang,[b] Yuxuan Yang,[b] Xiaodan Zhao,[b] Yanfeng Zhang,[a] Aimin Yang,[c] and Yilong Cheng*[ac]*

[a] Engineering Research Center of Energy Storage Materials and Devices, Ministry of Education, School of Chemistry, Xi'an Jiaotong University, Xi'an 710049, China

[b] Key Laboratory of Shaanxi Province for Craniofacial Precision Medicine Research, College of Stomatology, Xi'an Jiaotong University, Xi'an 710049, China

[c] Department of Nuclear Medicine, the First Affiliated Hospital of China, Xi'an Jiaotong University, Xi'an 710049, China

*E-mail: yilongcheng@mail.xjtu.edu.cn

## Experimental Section

### Materials

Acrylamide (AM) and acryloyl chloride were purchased from Adamas-beta Co., Ltd. (Shanghai, China). Ammonium persulfate (APS) was provided by Aladdin Bio-Chem Technology Co., Ltd. (Shanghai, China). Sodium bicarbonate, tetrahydrofuran (THF), and ethyl acetate were purchased from Guanghua Sci-Tech Co., Ltd. (Guangdong, China). Laponite XLG nanosheets (XLG) were obtained from Aoyuan New Material Technology Co., Ltd. (Shanghai, China). Carbon nanotubes (CNTs, GT-300) were supplied by Dazhan Nanomaterial Co., Ltd. (Shandong, China). 3-Acrylamidophenylboronic acid (APBA) was synthesized according to our previous work.[1] All the other chemical reagents were used without further purification.

### General characterization

The Fourier transform infrared (FT-IR) spectra were performed on a Nicolet iS50 FTIR spectrometer (Thermo Fisher Scientific, China). The surface morphologies and microstructures of the freeze-dried hydrogels were observed by a SU3500 scanning electron microscope (Tianmei Scientific Instruments Co., Ltd., China), and the high magnification images of hydrogel microstructures were obtained by a GeminiSEM 500 scanning electron microscope (Carl Zeiss (shanghai) Co., Ltd., China). The rheological properties of the hydrogels were evaluated by rotational rheometer (MCR302, Anton Paar Co., Ltd., Austria). X-ray diffraction (XRD) data were obtained from an X-ray diffractometer (XRD-6100, Shimadzu, Japan).

### Recovery property

To examine the recovery property, the hydrogel samples were first stretched to a predetermined 200% strain (crosshead speed: 50 mm $min^{-1}$) and then stretched again at the same rate after recovery for different times (0, 10, 20 min). The dissipated energy can be obtained by

calculating the area of the hysteresis loop. The recovery rate was defined as the ratio of energy dissipation and maximum stress after different recovery times to the first cycle.

**Cyclic tensile/compression test**

For cyclic loading-unloading tensile tests, the tensile rate was set at 50 mm $min^{-1}$. For cyclic loading-unloading compression tests, the compression rate was set at 10 mm $min^{-1}$. The energy dissipation can be obtained by calculating the area of the hysteresis loop. Besides, silicone oil was applied to the surface of the hydrogel to prevent evaporation. Humidifier and humidor were used around the sample to control the test humidity at 85% and central air conditioner was used to control the temperature at 25 °C.

**Tearing test**

For tearing tests, hydrogel samples were prepared into rectangular shape ($a_0$ = 20 mm, $b_0$ = 2 mm) with 8 mm initial notch and the tensile rate was set at 50 mm $min^{-1}$. The fracture energy was calculated according to the following formula:

$$\Gamma = \frac{U(L_c)}{a_0 b_0}$$

in which $L_c$ was the critical distance between fixtures when the notch became an operating crack. $U(L_c)$ was the integral area under the force-distance curve of the unnotched sample at the critical distance $L_c$. $a_0$ and $b_0$ represented the width and thickness of the sample, respectively.

**Swelling behavior**

The original mass of the hydrogel was weighed as $W_0$, and then the hydrogel was soaked in deionized water at different times. After wiping the surface of the hydrogel with filter paper to remove excess water carefully, the mass of the hydrogel was measured as $W_t$ at different times. The swelling ratio (*SR*) was calculated by the following formula:

$$SR = \frac{(W_t - W_0)}{W_0} \times 100\%$$

**Adhesion properties**

The adhesion properties of the hydrogel were determined by lap shear tests using a universal testing machine (CMT-1503, Shenzhen SANS Test Machine Co. Ltd., China) at room temperature. A hydrogel (10 ×10 × 1 $mm^3$) was sandwiched with two pieces of substrates to construct the adhesion joint and pressed at a pressure of 10 kPa for 10 minutes. The tensile speed was set at 5 mm $min^{-1}$. At least six samples were tested for each substrate.

**Conductivity test**

Electrical tests were conducted by electrochemical workstation CHI 650E (CH Instruments, Inc., USA). The electrochemical impendence spectroscopy (EIS) of the hydrogels was measured at a test frequency range from 0.1 to $10^6$ Hz with 10 mV voltage to obtain the resistance. Conductivities ($\sigma$, S $m^{-1}$) of the hydrogels were calculated by the following equation:

$$\sigma = \frac{L}{S \times R}$$

where $L$ (m), $S$ ($m^2$), and $R$ (Ω) represented the distance between the electrode sheets, the cross-sectional area, and the resistance of the hydrogel, respectively.

**Sensing properties**

The relative resistance changes ($\Delta R/R_0$) of the hydrogels under different strains and pressures were obtained using CMT-1503 electromechanical tester combined with electrochemical workstation CHI 650E. Similarly, attaching the hydrogels to human tissues can directly collect the relative resistance changes of the hydrogels produced by human movements. Notably, to avoid temperature interference with the electrical signals of hydrogels in response to stretching and compression stimuli during the monitoring of human motions, the hydrogels need to be

applied to human skins to achieve temperature equilibrium before the detection. The relative resistance changes ($\Delta R/R_0$) of the hydrogels under different temperature were carried out by electrochemical workstation CHI 650E combined with near-infrared (NIR) light as the hot source and infrared thermal imaging camera (Fluke-Ti401PRO) as temperature detector. The relative resistance changes were calculated by the following formula:

$$\Delta R/R_0 = \frac{(R - R_0)}{R_0} \times 100\%$$

in which $R$ and $R_0$ represented the test resistance and initial resistance of the hydrogels, respectively.

In addition, the gauge factor ($GF$) was used to measure the sensitivity of the hydrogel during the stretching process, which was calculated by the following formula:

$$GF = \frac{\Delta R/R_0}{\varepsilon}$$

where $\varepsilon$ represented the applied strain.

The sensitivity ($S$) was applied to measure the sensitivity of the hydrogel during the compression process, which was calculated by the following formula:

$$S = \frac{\Delta R/R_0}{\sigma}$$

where $\sigma$ represented the applied stress.

The temperature coefficient of resistance ($TCR$) can be used to measure thermal sensitivity of the hydrogel, which was calculated by the following formula:

$$TCR = \frac{\Delta R/R_0}{\Delta T}$$

in which $\Delta T$ represented the corresponding temperature change.

**Electromechanical responsiveness**

The electromechanical responsiveness of the hydrogels under tension and compression processes were conducted by CMT-1503 electromechanical tester combined with electrochemical workstation CHI 650E. The responding times for stretching and recovering processes were calculated by the hysteresis response time of the impedance to the strain in the tensile test with 50% strain and 200 mm $min^{-1}$ tensile speed.

***In vitro* cytotoxicity**

The 3-(4,5-dimethyl-2-thiazolyl)-2,5-diphenyltetrazolium bromide (MTT) assay was performed to test the cytotoxicity of the hydrogels. Fibroblast cells (L929) were cultured in DMEM supplemented with 10 % fetal bovine serum (FBS) and 1% penicillin-streptomycin (Hyclone) in a $CO_2$ incubator at 37 °C for 24 h. L929 cells were seeded in 96-well plate with a density of 2000 cells per well. After L929 cells adhered to the plate for 24 h, the culture medium was replaced by 100 μL hydrogel extract with the corresponding dilution extents. After 1, 2, and 3 days of incubation, 20 μL of MTT (5 mg $mL^{-1}$ in PBS) was added to each well and incubated for another 4 h. Eventually, the medium was replaced by 100 μL DMSO per well and the plate was shaken for 15 min. The absorbance was recorded by the Multiskan FC Microplate Reader (Thermo Fisher Scientific, USA) at 570 nm of wavelength. The cell viability was calculated as:

$$Cell\ viability\ (\%) = \frac{A_e - A_b}{A_c - A_b} \times 100\%$$

where $A_e$, $A_b$, and $A_c$ represented the absorbance of the experiment, background, and blank groups, respectively. The experiment was performed in triplicate.

Cell proliferation was further characterized by Live/Dead staining. L929 cells were seeded in the 24-well plate with a density of 5000 cells per well and cultured with DMEM medium

containing 10% FBS and 1% penicillin-streptomycin in a $CO_2$ incubator at 37 °C for 24 h. The hydrogel extract (25 mg $mL^{-1}$) was used to replace the medium and the cells were cultured for another 1, 2, and 3 days. Calcein-AM and propidium iodide were applied to stain the live and dead cells, respectively. The green (492 nm) and red (545 nm) fluorescence were observed under a fluorescent microscope (DMi8, Leica, Germany).

***In vivo* tissue biocompatibility**

Kunming mice (male, 6-8 weeks old, 25-30 g) were bought from the experimental animal center of Xi'an Jiaotong University. All animal protocols in this study were approved by the Ethical Committee of Xi'an Jiaotong University. All the animal experiments were performed in compliance with the guidelines for the Institutional Animal Care and Use Committee (IACUC) established by the Health Science Center of Xi'an Jiaotong University. The case number of ethics is 2021-1080. P($AM_3$-$APBA_{0.06}$)$XLG_{1.0}$/CNTs hydrogel was washed three times with PBS buffer (0.01 M) before subcutaneous implantation. The back of Kunming mice was treated with local dehairing and disinfection, and an incision of about 1 cm was made on the back of the mice after anesthetization. The hydrogels with 6 mm diameter and 2 mm thickness were then subcutaneously implanted into mice. At 3, 7, 14, and 28 days, the surrounding tissues were collected, and histocompatibility was evaluated by hematoxylin and eosin (H&E) staining.

***In vivo* wound closure**

A 1 cm full-thickness mice dorsal skin wound was created for the in vivo wound closure test. The skin wound was treated by P($AM_3$-$APBA_{0.06}$)$XLG_{1.0}$/CNTs hydrogel, P($AM_3$-$APBA_{0.06}$)$XLG_{1.0}$ hydrogel, and suture, and the untreated wound was used for comparison. After 1 and 3 weeks of recovery, photographs of the wound site were taken, and H&E staining was used to assess the wound closure.

**Wound healing monitoring**

After anesthesia and depilation, a full-thickness skin wound (1 cm in length) was created on the back of each mouse ( 6-8 weeks old male Kunming mice, 25-30 g). The photographs of the skin defects in each group were captured by a digital camera on day 3 and 7, while the temperature of the wound site was recorded by an infrared thermal imaging camera (Fluke-Ti401PRO). The full-thickness skin wound tissues were collected, and immunofluorescence staining of CD11b and TNF-α were used to study wound healing and inflammatory responses. The wound-healing process was further evaluated by monitoring the temperature of the wound site with an electrochemical workstation (CHI 650E). After anesthesia for 30 min, P($AM_3$-$APBA_{0.06}$)$XLG_{1.0}$/CNTs hydrogel was adhered to wound site to monitor the change of temperature, and the relative change of $\Delta R/R_0$ on certain day was calculated by the equation below:

$$relative\ change\ of^{\Delta R}/_{R_0}(\%) = \frac{^{\Delta R}/_{R_0}\ of\ W - \ ^{\Delta R}/_{R_0}\ of\ C}{^{\Delta R}/_{R_0}\ of\ C} \times 100\%$$

in which *W* and *C* represented wound and control groups, respectively.

**Results**

**Video S1. Puncture resistance of P($AM_3$-$APBA_{0.06}$)$XLG_{1.0}$/CNTs hydrogel.**

**Video S2. Elasticity of a hydrogel ball ( 16 mm in diameter).**

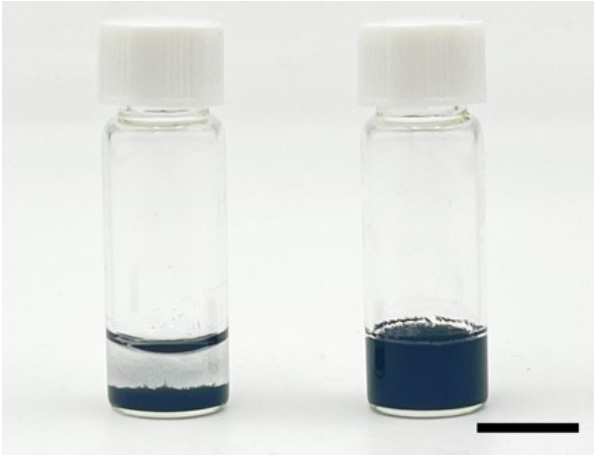

**Fig. S1** Photographs of the P($AM_3$-$APBA_{0.06}$)CNTs and P($AM_3$-$APBA_{0.06}$)$XLG_{1.0}$/CNTs hydrogels (scale bar = 1 cm).

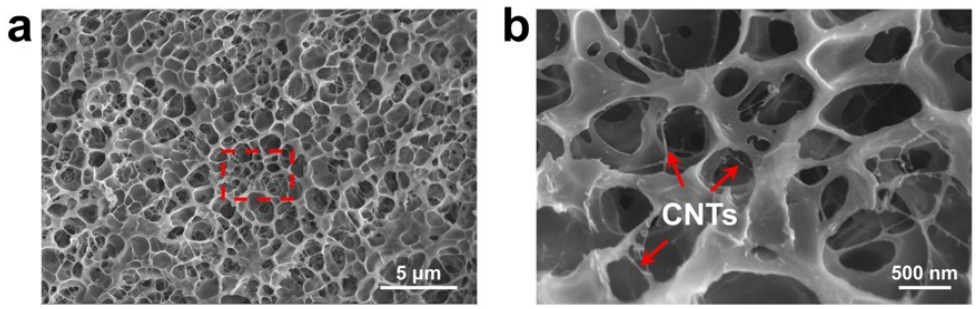


**Fig. S2** SEM images with high magnification of P($AM_3$-$APBA_{0.06}$)$XLG_{1.0}$/CNTs hydrogel.

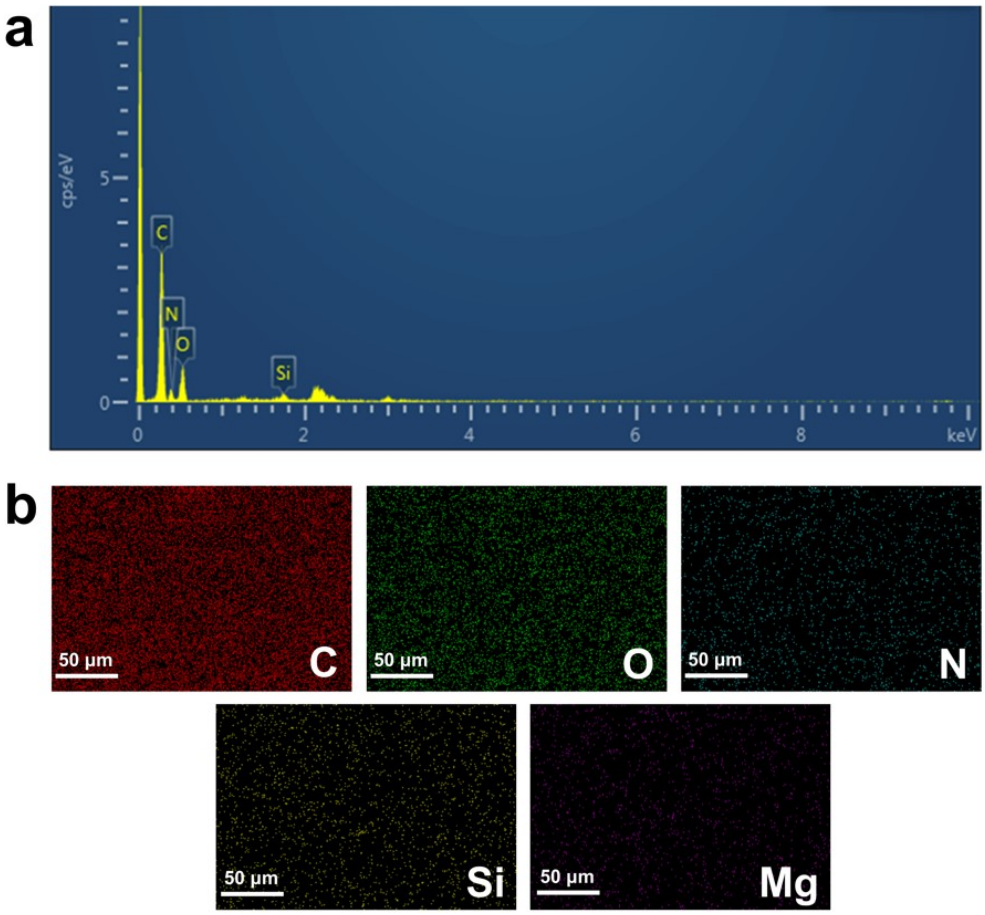


**Fig. S3** EDS spectrum (a) and elemental mapping images (b) of P($AM_3$ $APBA_{0.06}$)$XLG_{1.0}$/CNTs hydrogel.

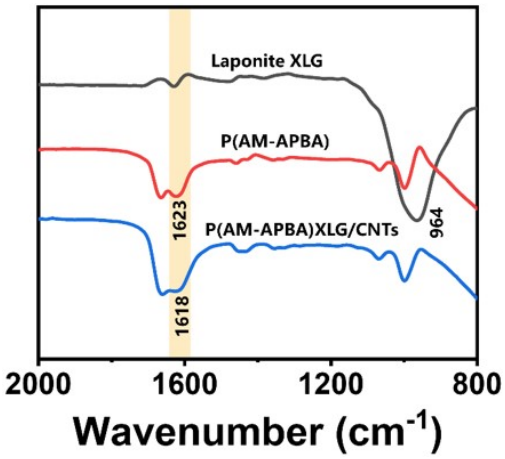


**Fig. S4** FT-IR spectra of Laponite XLG powder, P($AM_3$-$APBA_{0.06}$) and P($AM_3$-$APBA_{0.06}$)$XLG_{1.0}$/CNTs hydrogels.

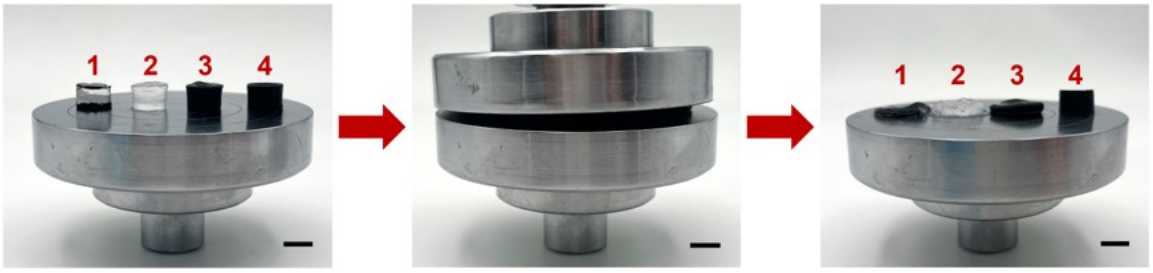


**Fig. S5** Photographs of the $PAM_3$/CNTs (1), $PAM_3/XLG_{1.0}$ (2), $PAM_3/XLG_{1.0}$/CNTs (3), and $P(AM_3\text{-}APBA_{0.06})XLG_{1.0}$/CNTs (4) hydrogels recovered from compression (scale bar = 1 cm).

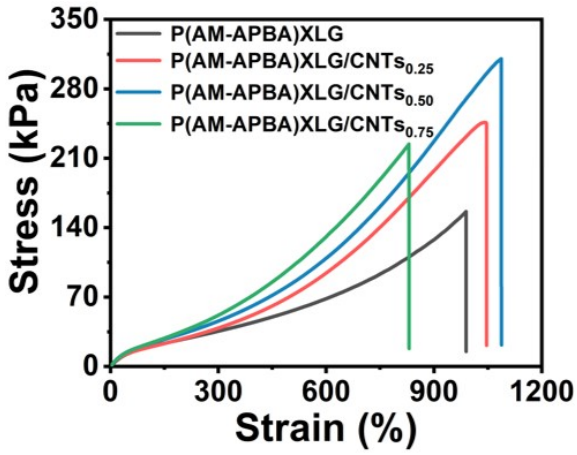


**Fig. S6** Tensile stress-strain curves of $P(AM_3\text{-}APBA_{0.06})XLG_{1.0}$/CNTs hydrogels with different CNTs contents.

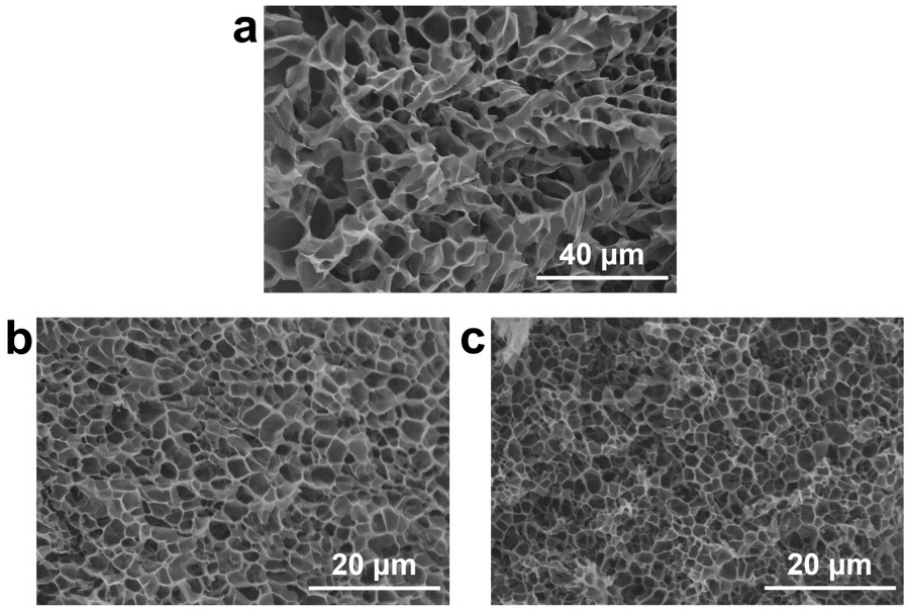


**Fig. S7** SEM images of P($AM_3$-$APBA_{0.06}$)$XLG_{1.0}$ (a), P($AM_3$-$APBA_{0.06}$)$XLG_{0.5}$/CNTs (b), and P($AM_3$-$APBA_{0.06}$)$XLG_{1.5}$/CNTs (c) hydrogels.

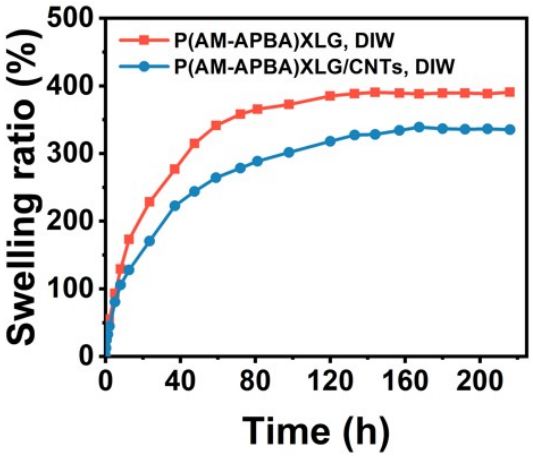


**Fig. S8** Swelling behaviors of P($AM_3$-$APBA_{0.06}$)$XLG_{1.0}$/CNTs and P($AM_3$-$APBA_{0.06}$)$XLG_{1.0}$ hydrogels.

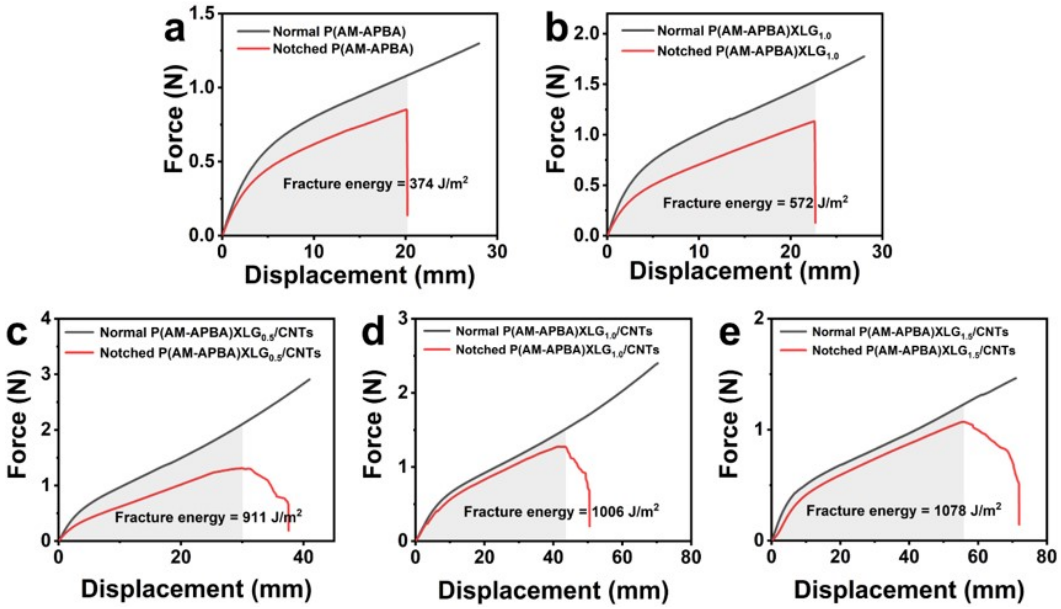


**Fig. S9** The force-displacement curves of the notched and unnotched $P(AM_3\text{-}APBA_{0.06})$ (a), $P(AM_3\text{-}APBA_{0.06})XLG_{1.0}$ (b), $P(AM_3\text{-}APBA_{0.06})XLG_{0.5}$/CNTs (c), $P(AM_3\text{-}APBA_{0.06})XLG_{1.0}$/CNTs (d), and $P(AM_3\text{-}APBA_{0.06})XLG_{1.5}$/CNTs (e) hydrogel samples.

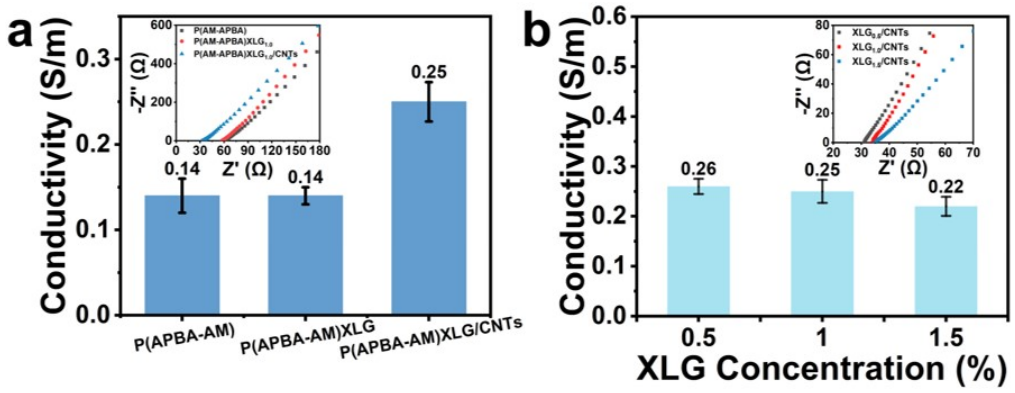


**Fig. S10** Conductivities of P($AM_3$-$APBA_{0.06}$), P($AM_3$-$APBA_{0.06}$)$XLG_{1.0}$, and P($AM_3$-$APBA_{0.06}$)$XLG_{1.0}$/CNTs hydrogels (a) and P($AM_3$-$APBA_{0.06}$)$XLG_z$/CNTs hydrogels with various XLG concentrations (b).

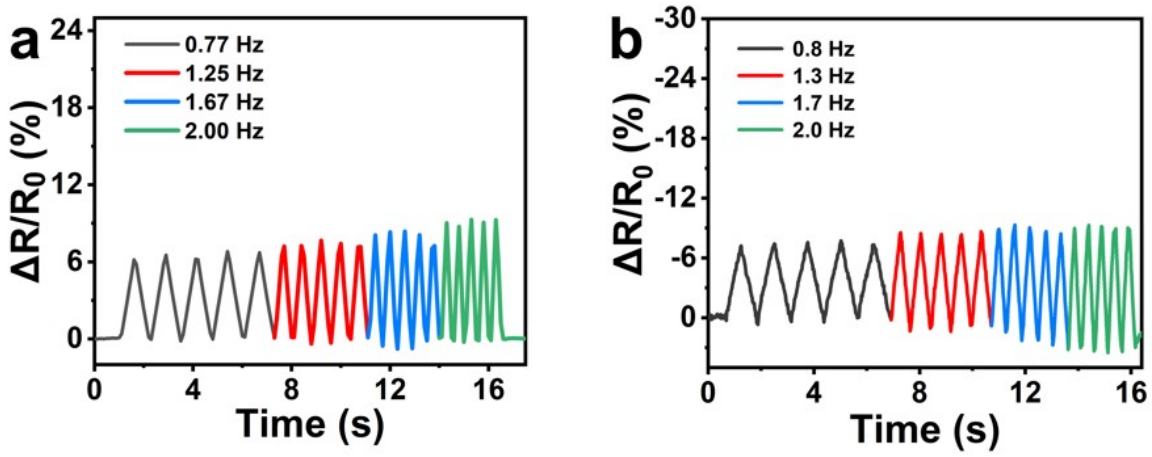


**Fig. S11** Relative resistance changes of P($AM_3$-$APBA_{0.06}$)$XLG_{1.0}$/CNTs hydrogel at different strain (a) and compression (b) frequencies.

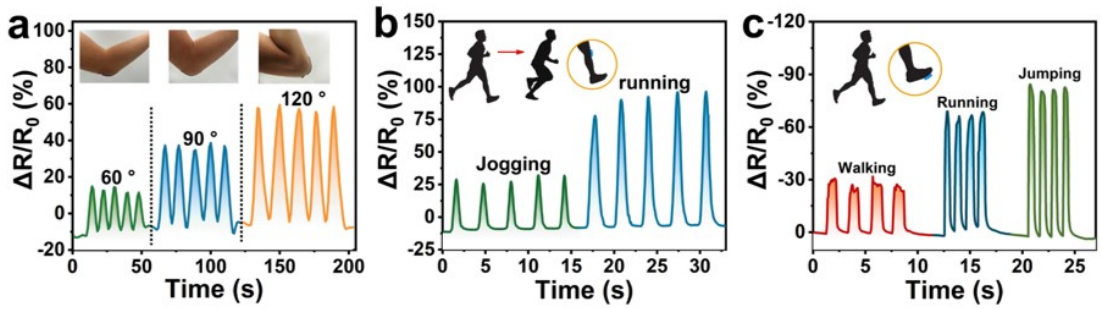


**Fig. S12** Relative resistance changes of P($AM_3$-$APBA_{0.06}$)$XLG_{1.0}$/CNTs hydrogel responding to elbow joint (a) and knee joint (b) bending under different motion degrees. c) The monitor of walking, running, and jumping by P($AM_3$-$APBA_{0.06}$)$XLG_{1.0}$/CNTs hydrogel.

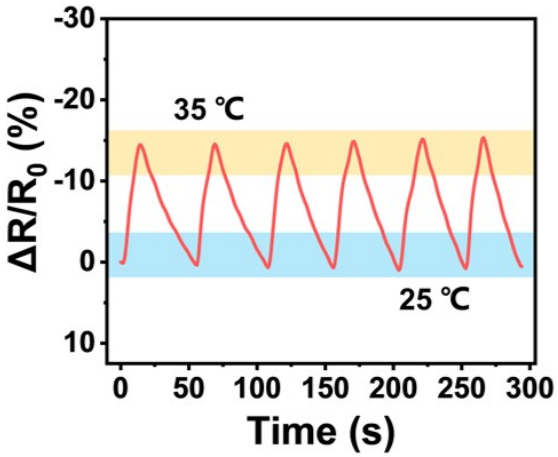


**Fig. S13** Cyclic resistance changes of P($AM_3$-$APBA_{0.06}$)$XLG_{1.0}$/CNTs hydrogel upon heating (35 °C) and cooling (25 °C) cycles.

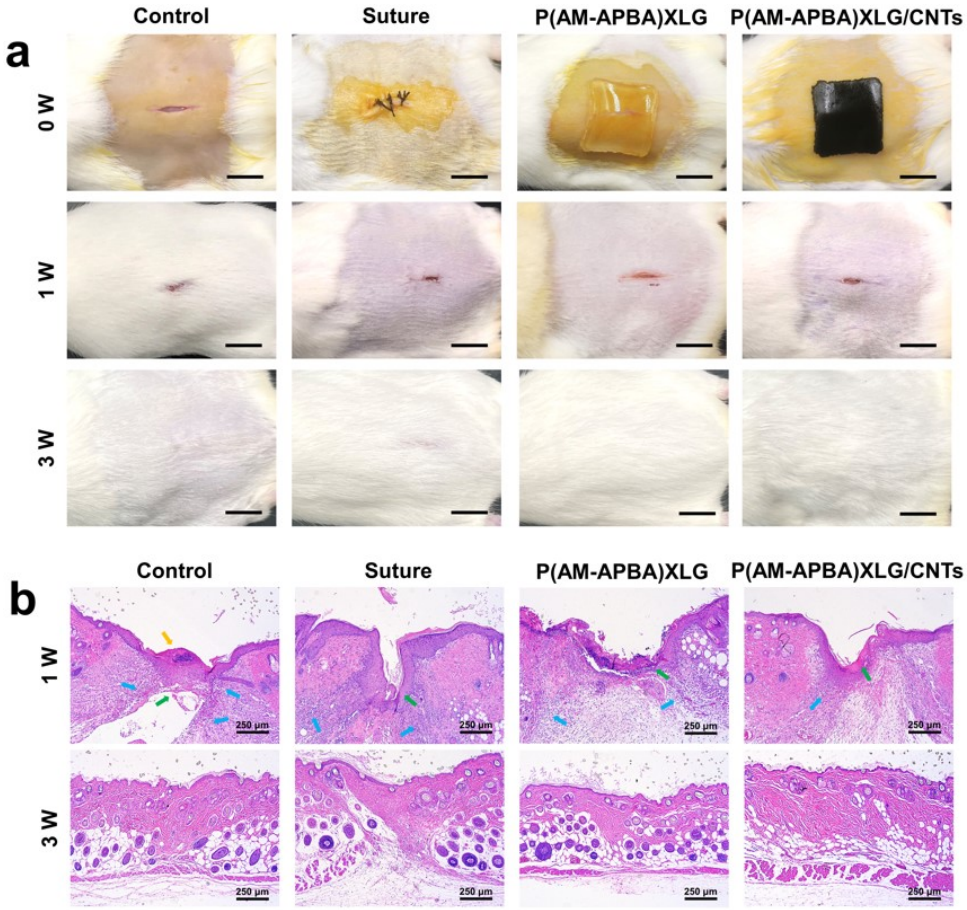


**Fig. S14** a) Photographs of the skin incision healing on week 0, week 1, and week 3 for P($AM_3$-$APBA_{0.06}$)$XLG_{1.0}$/CNTs hydrogel, P($AM_3$-$APBA_{0.06}$)$XLG_{1.0}$ hydrogel, suture, and control groups (scale bar = 1 cm). b) Histological evaluation of regenerated skin tissues for P($AM_3$-$APBA_{0.06}$)$XLG_{1.0}$/CNTs hydrogel, P($AM_3$-$APBA_{0.06}$)$XLG_{1.0}$ hydrogel, suture, and control groups on week 1 and week 3. Yellow, blue, and green arrows represent eschars, inflammatory cells, and unhealed wounds, respectively.

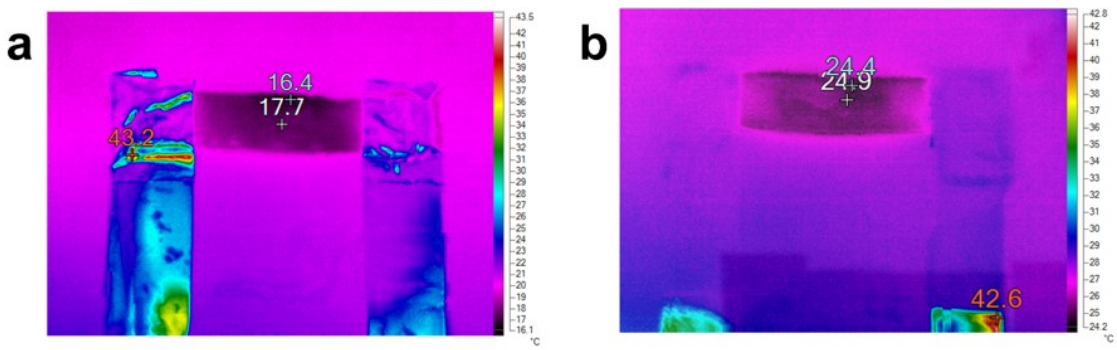


**Fig. S15** Infrared thermal images of P($AM_3$-$APBA_{0.06}$)$XLG_{1.0}$/CNTs hydrogel to detect room temperature on day 3 (a) and 7 (b).

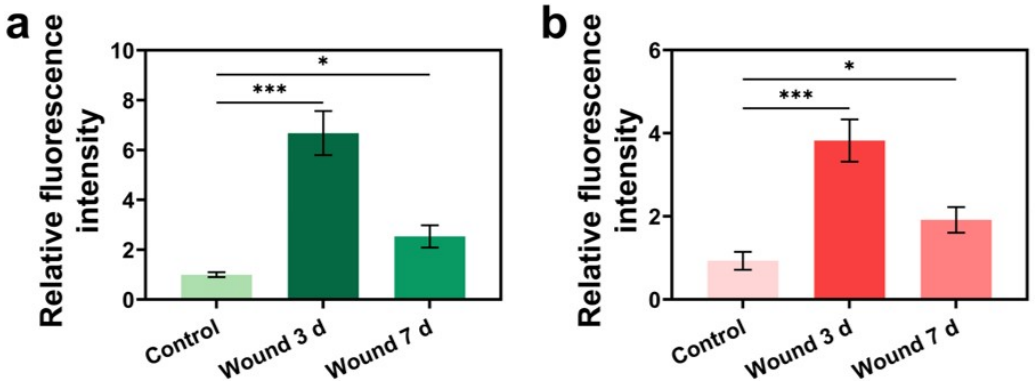


**Fig. S16** Quantitative analysis of the relative fluorescence intensity of TNF-α (a) and CD11b (b) for different groups. Data are presented as mean ± SD (n = 3 per group); *$p < 0.05$; **$p < 0.01$; ***$p < 0.001$.

**Table S1.** Comparison of comprehensive performances of the hydrogel in this work with the reported hydrogel-based sensors.

| Components | Tensile strength (kPa) | Elongation at break (%) | Toughness ($MJ/m^3$) | Hysteresis ratio & number of cycles | Maximum GF | TCR (% $°C^{-1}$) | Detection limit | | | Ref. |
|---|---|---|---|---|---|---|---|---|---|---|
| | | | | | | | Strain (%) | Pressure (kPa) | Temperature (°C) | |
| **P(AM-APBA)XLG/CNTs** | **323** | **1200** | **1.5** | **9% / 1000** | **9.43** | **-1.24** | **1-300** | **1-80** | **25-50** | **This work** |
| CH-OSNP | 110 | 300 | N/A | 24% / 5 | N/A | -1.43 | N/A | 0.2-10 | 35-40 | 2 |
| PSB/CMC-$Ag^+$ | 38 | 163 | N/A | N/A | N/A | -1.70 | N/A | N/A | 35-50 | 3 |
| QAAH | 290 | 2200 | N/A | N/A | N/A | -1.53 | N/A | N/A | 30-70 | 4 |
| CH-GT | 1280 | 83 | N/A | N/A | N/A | -0.83 | N/A | 1.25-10 | 20-100 | 5 |
| MXenes bonded hydrogel | 2280 | 375 | N/A | 11% / 4 | 5.7 | -0.84 | 10-50 | N/A | 40-80 | 6 |
| PTTGC | 355 | 870 | N/A | 10% / 50 | 1.62 | -1.05 | 5-150 | N/A | 25-85 | 7 |
| GDIH | 165 | 991 | N/A | 46% / 10 | 2.24 | N/A | 15-40 | 3-5 | N/A | 8 |
| PACG-M | 120 | 918 | 0.59 | 2% / 10 | 3.93 | N/A | 1-600 | 0.08-3.2 | N/A | 9 |
| HK-L-PAAm | 78 | 2370 | 0.65 | 15% / 5 | 6.20 | N/A | 0.5-100 | 2-35 | N/A | 10 |
| TA@HAPNWs-PVA(EG/W) | 360 | 480 | 0.94 | N/A | 2.84 | N/A | 50-300 | N/A | N/A | 11 |
| DN-FT-HCl | 376 | 337 | 0.52 | 7% / 20 | 3.36 | N/A | 1-200 | N/A | N/A | 12 |
| SGC | 90 | 1380 | 0.40 | 9% / 20 | 14.50 | N/A | 0.2-500 | N/A | N/A | 13 |
| P(AMPS/AAm)-CS | 111 | 2839 | 1.30 | 31% / 10 | 7.08 | N/A | 3-70 | N/A | N/A | 14 |

| | | | | | | | | | | |
|---|---|---|---|---|---|---|---|---|---|---|
| P(MEA-AA)-GH | 175 | 1260 | N/A | 8% / 10 | 3.40 | N/A | 0.2-500 | 0.7-68 | N/A | 15 |
| PAAc/$SiO_2$-g-PAAm | 35 | 1500 | N/A | 13% / 5 | 5.86 | N/A | 50-400 | 0.2-5 | N/A | 16 |
| P(AA-APA)-$Fe^{3+}$ | 336 | 1048 | 1.32 | 31% / 1000 | 7.95 | N/A | 2.5-300 | 1-80 | N/A | 17 |

**Table S2.** Comparison of tissue adhesiveness of the hydrogel in this work with the reported hydrogel-based sensors.

| Components | Adhesion strength (kPa) | Ref. |
|---|---|---|
| **P(AM-APBA)XLG/CNTs** | **8.0** | **This work** |
| P(AM-APBA)NaCl | 7.5 | 1 |
| SGC | 2.5 | 13 |
| Al-IL | 3.7 | 18 |
| PAM/Agar/TA-B | 5.9 | 19 |
| AD-TENG | 3.0 | 20 |
| CMCS-PA@Fe | 2.8-8.9 | 21 |
| PNIPAM/L/CNT | 6.1 | 22 |
| PAA/TA@HC/$Fe^{3+}$ | 8.5 | 23 |
| PNA/PVP/TA/$Fe^{3+}$ | 1.2 | 24 |
| poly(AA-co-AM)/AP | 12.6 | 25 |

## References


1 K. Xu, K. Shen, J. Yu, Y. Yang, Y. Wei, P. Lin, Q. Zhang, C. Xiao, Y. Zhang and Y. Cheng, *Chem. Mater.*, 2022, **34**, 3311-3322.

2 X. Liu, S. Tian, S. Xu, W. Lu, C. Zhong, Y. Long, Y. Ma, K. Yang, L. Zhang and J. Yang, *Biosens. Bioelectron.*, 2022, **214**, 114528.

3 Y. Long, M. Bai, X. Liu, W. Lu, C. Zhong, S. Tian, S. Xu, Y. Ma, Y. Tian, H. Zhang, L. Zhang and J. Yang, *Carbohydr. Polym.*, 2022, **297**, 119974.

4 X. Shi and P. Wu, *Small*, 2021, **17**, 2101220.

5 J. Liu, H. Wang, T. Liu, Q. Wu, Y. Ding, R. Ou, C. Guo, Z. Liu and Q. Wang, *Adv. Funct. Mater.*, 2022, **32**, 2204686.

6 H. Liu, C. Du, L. Liao, H. Zhang, H. Zhou, W. Zhou, T. Ren, Z. Sun, Y. Lu, Z. Nie, F. Xu, J. Zhu and W. Huang, *Nat. Commun.*, 2022, **13**, 3420.

7 Y. Zhu, L. Lin, Y. Chen, Y. Song, W. Lu and Y. Guo, *ACS Appl. Mater. Interfaces*, 2020, **12**, 56470-56479.

8 H. Fu, B. Wang, J. Li, J. Xu, J. Li, J. Zeng, W. Gao and K. Chen, *Mater. Horiz.*, 2022, **9**, 1412-1421.

9 S.-N. Li, Z.-R. Yu, B.-F. Guo, K.-Y. Guo, Y. Li, L.-X. Gong, L. Zhao, J. Bae and L.-C. Tang, *Nano Energy*, 2021, **90**, 106502.

10 Y. Gao, S. Gu, F. Jia, Q. Wang and G. Gao, *Chem. Eng. J.*, 2020, **398**, 125555.

11 J. Wen, J. Tang, H. Ning, N. Hu, Y. Zhu, Y. Gong, C. Xu, Q. Zhao, X. Jiang, X. Hu, L. Lei, D. Wu and T. Huang, *Adv. Funct. Mater.*, 2021, **31**, 2011176.

12 J. Ren, Y. Liu, Z. Wang, S. Chen, Y. Ma, H. Wei and S. Lü, *Adv. Funct. Mater.,* 2022, **32**, 2107404.

13 Z. Wang, H. Zhou, D. Liu, X. Chen, D. Wang, S. Dai, F. Chen and B. B. Xu, *Adv. Funct. Mater.*, 2022, **32**, 2201396.

14 R. Jin, J. Xu, L. Duan and G. Gao, *Carbohydr. Polym.*, 2021, **268**, 118240.

15 X. Liu, Q. Zhang and G. Gao, *ACS Nano*, 2020, **14**, 13709-13717.

16 X. Yu, Y. Zheng, H. Zhang, Y. Wang, X. Fan and T. Liu, *Chem. Mater.*, 2021, **33**, 6146-6157.

17 K. Shen, K. Xu, M. Zhang, J. Yu, Y. Yang, X. Zhao, Q. Zhang, Y. Wu, Y. Zhang and Y. Cheng, *Chem. Eng. J.*, 2023, **451**, 138525.

18 X. Zhang, C. Cui, S. Chen, L. Meng, H. Zhao, F. Xu and J. Yang, *Chem. Mater.*, 2022, **34**, 1065-1077.

19 H. Lei, J. Zhao, X. Ma, H. Li and D. Fan, *Adv. Funct. Mater.*, 2021, **10**, 2101089.

20 X. Guo, F. Yang, X. Sun, Y. Bai, G. Liu, W. Liu, R. Wang and X. He, *Adv. Funct. Mater.*, 2022, **32**, 2201230.

21 Y. Min, R. Han, G. Li, X. Wang, S. Chen, M. Xie and Z. Zhao, *Adv. Funct. Mater.*, 2023, 2212803.

22 Z. Deng, T. Hu, Q. Lei, J. He, P. X. Ma and B. Guo, *ACS Appl. Mater. Interfaces*, 2019, **11**, 6796-6808.

23 X. Gong, C. Fu, N. Alam, Y. Ni, L. Chen, L. Huang and H. Hu, *Biomacromolecules*, 2022, **23**, 2272-2279.

24 Q. Pang, H. Hu, H. Zhang, B. Qiao and L. Ma, *ACS Appl. Mater. Interfaces*, 2022, **14**, 26536-26547.

25 H. Zhou, J. Lai, B. Zheng, X. Jin, G. Zhao, H. Liu, W. Chen, A. Ma, X. Li and Y. Wu, *Adv. Funct. Mater.*, 2022, **32**, 2108423.